4D Evolution of $Cr_{23}C_6$ Precipitates in Neutron Irradiated and Annealed HT-UPS Steel Observed Via Synchrotron Micro-computed Tomography

Sri Tapaswi Nori[a,†], Alejandro Figueroa Bengoa[a,†], Jonova Thomas[a], James Hunter[b], Peter Kenesei[c], Jun-Sang Park[c], Jonathan Almer[c], Maria A. Okuniewski[a*]

[a]School of Materials Engineering, Purdue University, West Lafayette, IN, USA
[b]Los Alamos National Laboratory, Los Alamos, NM, USA
[c]Advanced Photon Source, Argonne National Laboratory, Lemont, IL, USA

[†]These authors contributed equally.

[*]Corresponding author. Email address: mokuniew@purdue.edu (Maria A. Okuniewski)

Abstract

High temperature-ultrafine precipitate strengthened (HT-UPS) steel is a potential structural material for advanced nuclear reactors; however, its irradiation response is not well understood. This research provides insight into irradiation-induced effects, such as precipitate evolution mechanisms and four-dimensional morphological evolution, in HT-UPS steel using synchrotron micro-computed tomography. Identical specimens were characterized pre-irradiation and post-irradiation following neutron exposure up to 0.3 displacements per atom at 600 °C. Irradiation effects were also differentiated from the annealing response of precipitates. Following neutron irradiation, the average $Cr_{23}C_6$ precipitate size reduced, affected by the synergy of nucleation and growth, ballistic dissolution, and inverse coarsening, which was observed at fluences an order of magnitude lower than previously observed. Annealing at 600 °C for 32 h increased the average $Cr_{23}C_6$ precipitate size and decreased the phase fraction, attributed to precipitate coarsening. The precipitate morphology evolution and resultant mechanisms can be utilized to parameterize and validate microstructural models simulating radiation damage or annealing.

Figure Abstract

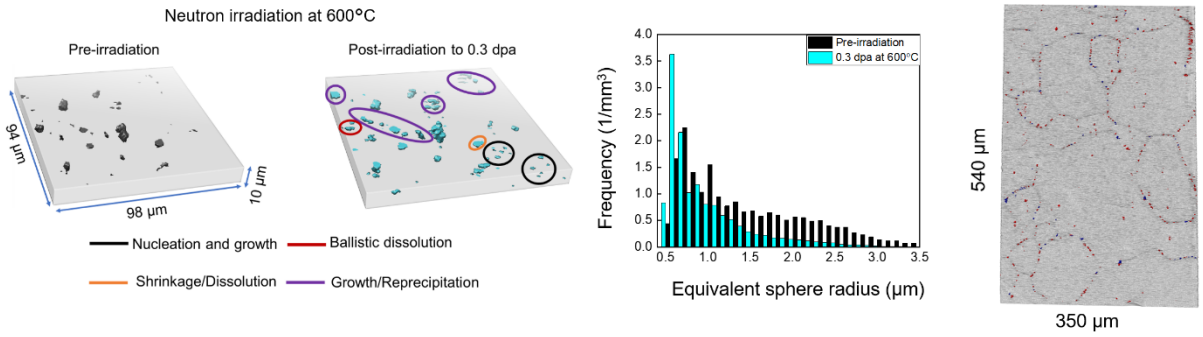

Keywords: radiation effects, nuclear materials; neutron irradiation; annealing; X-ray tomography; steel

Biography

Dr. Maria Okuniewski is an assistant professor in the School of Materials Engineering at Purdue University, where she also holds a courtesy appointment with the School of Nuclear Engineering. Prior to joining Purdue, she held a staff position for eight years as a research and development scientist and engineer at Idaho National Laboratory. During her time in Idaho, she was also an adjunct faculty member at Idaho State University in the Department of Nuclear Engineering and Health Physics. She obtained her M.S. (2004) and Ph.D. (2008) degrees in Nuclear Engineering at the University of Illinois at Urbana-Champaign. Dr. Okuniewski's research focuses on the connections between processing, microstructure, mechanical properties, and performance of nuclear materials and fuels at the atomistic to mesoscale levels. Her research utilizes experimental and modeling techniques in a complementary fashion. She is the recipient of the U.S. Department of Energy Fuel Cycle Research and Development Excellence Award (2013), Oak Ridge Associated Universities (ORAU) Ralph E. Powe Junior Faculty Award (2017), and the American Nuclear Society Mary Jane Oestmann Professional Women's Award (2020).

Introduction

High temperature-ultrafine precipitate strengthened (HT-UPS) steel is a type of austenitic stainless steel developed in the 1980s primarily for structural material applications in advanced fossil fuel plants [1]. HT-UPS steel demonstrated higher strength and creep resistance at elevated temperatures (> 600 °C) compared to traditional austenitic stainless steels, such as the 300 series [1–7]. In particular, creep properties of HT-UPS steel are comparable to Ni-based superalloys [3,4]. The superior mechanical properties of HT-UPS steel are primarily attributed to the formation of nanometer-sized metal carbide (MC) (M: Ti, Nb, and V) precipitates at temperatures above 600°C. The MC precipitates preclude both glide and climb forms of dislocation movement by pinning during thermal creep [2–4,6,7]. Creep studies conducted at 700 °C and 170 MPa for 18,000 h indicated the formation of stable MC precipitates, and resistance to creep-induced voids, as well as harmful sigma and Lave phases [2,4]. Formation of stable MX (M: Ti, Nb; X: C, N) precipitates (~ 80 nm), along with $M_{23}C_6$ precipitates (> 100 nm) were identified using thermodynamic extremum principles and classical nucleation theory following aging at 700 °C for 100,000 h [8]. The MX phase fraction slightly increased after 1 h of aging, whereas the $M_{23}C_6$ phase fraction peaked following 3 h of aging followed by a consistent decrease throughout the duration of the aging treatment [8].

The microstructural characteristics of HT-UPS steel are also desirable for structural materials in advanced nuclear reactors [2,3]. Specifically, MC and $M_{23}C_6$ precipitates act as point defect annihilation centers, and MC precipitates serve as sites to trap helium (He) atoms [2,6,9–11]. This behavior results from the positive lattice misfit between the precipitate and matrix, with values of up to 25% for the MC precipitates [11,12]. Therefore, HT-UPS steel may be able to minimize critical nuclear reactor structural material problems such as irradiation-induced void swelling and He embrittlement [2–4,11,12]. In addition, HT-UPS steel was found to be compatible for use in sodium fast reactors, another advanced nuclear reactor type under consideration for new builds [13].

Currently, scant information exists for the neutron irradiation behavior of HT-UPS steels regarding mechanical and microstructural responses [14–17]. Post-irradiation (3 displacements per atom, or dpa, at 400 °C) in-situ tensile studies using far-field high-energy diffraction microscopy (FF-HEDM) indicated irradiation hardening and lattice strain anisotropy [17]. Defect studies of neutron irradiated (3 dpa at 500 ºC) HT-UPS steel, identified Frank loops, but did not resolve the presence of voids using transmission electron microscopy [14]. Grain studies of the identical irradiation conditions, via FF-HEDM, demonstrated sharpening of two-fiber texture, a reduction in the volume-weighted lattice constant, and no significant changes in grain sizes following irradiation [16]. Limited precipitate studies of the MX and $M_{23}C_6$ phases have also been conducted. For example, an atom probe tomography study depicted clusters rich in Ti and Nb in neutron irradiated (3 dpa at 500 ºC) HT-UPS steel [14]. More recently, synchrotron-based X-ray absorption near-edge spectroscopy (XANES) revealed an increase in the radiation-enhanced $Cr_{23}C_6$ phase following neutron irradiation up to 0.3 dpa at 600 ºC [15]. However, the XANES study did not identify the mechanisms responsible for the increase in the $Cr_{23}C_6$ phase, nor did it spatially locate and quantify the $Cr_{23}C_6$ precipitates in the HT-UPS steel microstructure, thus motivating the current research.

In the current research, synchrotron-based X-ray micro-computed tomography (μ-CT) was employed to understand four-dimensional (4D) $Cr_{23}C_6$ precipitate evolution in HT-UPS steel before and after low fluence neutron irradiations up to 0.3 dpa (1.08×10^{21} n/cm^2) at 600 °C by evaluating precipitate spatial distributions and geometries within identical specimens. A propagation-based phase-contrast μ-CT technique was utilized, which relies on the phase contrast of X-rays that arise due to changes in refractive indices in a material [18,19]. The refractive index is proportional to the electron density and mass density of the features in a material, thus enabling the effective characterization of precipitates. Understanding precipitate evolution is critical since they can serve as centers to pin dislocation and grain boundary movement, as well as trap point defects and He gas atoms. As a part of this research, precipitate evolution was also evaluated before and after annealing at 600 °C in HT-UPS steel. Thus, a unique, comparative examination characterizes thermal effects separately from neutron effects for precipitate evolution.

In general, neutron radiation damage studies that characterize the evolution of the identical microstructure by comparing pre-irradiation and post-irradiation microstructures of the same specimen are practically non-existent due to the complexity and cost of the experiments, as well as the previous lack of advanced nuclear materials sample preparation and characterization

techniques. Therefore, this study will provide 4D microstructural insight into precipitate evolution, which can be important to tailoring a material's radiation or thermal response, as well as producing parameterization and validation data for mesoscale codes (e.g., phase field).

Results

Precipitate Segmentation

Two separate investigations were performed to characterize precipitate evolution using synchrotron μ-CT imaging of HT-UPS steel subjected to neutron irradiation or thermal treatments. The μ-CT imaging produced radiographs, which were reconstructed to produce tomographs and then segmented to identify precipitates. Due to the small volume fraction of second phase precipitates in the specimens, traditional model-based segmentation, such as global thresholding, is ineffective and inaccurate [20]. Therefore, an edge-based approach (e.g., Sobel edge-filter) was utilized to segment the features while maintaining the attenuation contrast expected [20,21]. To accomplish this a two-part segmentation procedure was created consisting of an initial Sobel edge segmentation [20] followed by a Chan-Vese iterative area contouring algorithm [21] to verify and define the boundaries of the precipitates. A previous study on the identical HT-UPS specimens used in this investigation revealed two major precipitate phases, $Cr_{23}C_6$ and MX [15], using synchrotron X-ray diffraction. The precipitates observed in the current study are $Cr_{23}C_6$ since MX precipitates are only a few nanometers in size [14], thus are below the resolution range of μ-CT (0.40 - 3.2 μm^3) in this study. In austenitic stainless steels, $Cr_{23}C_6$ precipitates may also be void and/or He bubble associated, post-irradiation [22]; however, it is difficult to discern co-located voids and bubbles via μ-CT.

Figure 1 exemplifies the sequential representation of the precipitate segmentation procedure on a two-dimensional (2D) slice, as shown in Figs. 1 (a) - (c), and a 3D volume, as shown in Figs. 1 (d) – (f) of the pre-annealed HT-UPS steel specimen. Figure 1 (a) represents a slice of the tomograph with the grayscale corresponding to the attenuation of the material. Figure 1 (b) illustrates the edge segmentation of the features in the 2D slice using a Sobel edge filter [20] with white outlines corresponding to the segmented edges of the precipitates. Figure 1 (c) depicts the segmented precipitates represented in white after implementing the Chan-Vese algorithm [21] on the 2D slice. Thus, the precipitates were successfully segmented in all specimens, pre-irradiation, post-irradiation, pre-annealing, and post-annealing, as demonstrated in Fig. 1.

The 3D tomography showing the isosurfaces of the segmented precipitates and the boundaries of the illuminated volumes are displayed in Fig. 2. Figures 2 (a) and (b) depict the tomographs for pre-irradiation and post-irradiation of 0.003 dpa at 600 °C, respectively, while Figs. 2 (c) and (d) show the tomographs for pre-irradiation and post-irradiation of 0.3 dpa at 600 °C. Similarly, Figs. 2 (e) – (h) illustrate the tomographs for pre-annealing and post-annealing for 3.2 h, 6.4 h, and 32 h at 600 °C. Fig. 2 indicates the presence of the precipitates dispersed throughout the specimens for all conditions of the HT-UPS steel specimens. The segmented $Cr_{23}C_6$ precipitates were further analyzed to identify various radiation and thermally induced phenomena or mechanisms controlling size evolution (e.g., nucleation and growth, ballistic dissolution,

shrinkage/dissolution, and growth/reprecipitation), as well as to understand the corresponding morphological evolution, specifically volume, equivalent sphere radii, sphericity, precipitate phase fraction or V_V, and the precipitate surface area per unit volume or S_V. Since identical samples were characterized before and after irradiation or annealing, effectively capturing the same precipitates, any fluctuation in the size distribution (including the average and standard deviation of volume) and geometry are assumed to be a result of precipitate evolution rather than sample-to-sample variability. The average error is not discussed due to the large quantity (over 500,000 per sample) of precipitates analyzed in this study, resulting in the average error equaling approximately zero. The sheer number of precipitates present is evident in Fig. 2, which represents only one-half to one-third of the volume analyzed per sample. Note that the equivalent sphere radii will be referred to as radii in the remainder of the text.

Precipitate Evolution Phenomena

Figures 3 (a) - (d) show selected regions of interest of the 3D μ-CT segmented tomographs, illustrated in Figs. 2 (a) - (d), identifying precipitate evolution phenomena that occurred following neutron irradiation. Figures 3 (a) and (b) represent the identical specimen region pre-irradiation and post-irradiation of 0.003 dpa at 600 ºC and Figs. 3 (c) and (d) illustrate the identical specimen region pre-irradiation and post-irradiation of 0.3 dpa at 600 °C. Characterization of identical specimens was performed before and after neutron irradiations, thus enabling a comprehensive understanding of the 3D precipitate evolution.

The $Cr_{23}C_6$ precipitate evolution phenomena, such as nucleation and growth (black ellipses), ballistic dissolution (red ellipses), shrinkage/dissolution (orange ellipses), and growth/reprecipitation (purple ellipses), occurred post-irradiation in both 0.003 dpa and 0.3 dpa specimens, as shown in Figs. 3 (a) to (d). The instances of nucleation and growth phenomena were identified by the formation of new $Cr_{23}C_6$ precipitates post-irradiation that were not found in the pre-irradiated specimen. The ballistic dissolution or recoil dissolution [10] phenomenon was recognized when a precipitate in the pre-irradiation state breaks into multiple fragments post-irradiation, indicating that neutron bombardment ballistically ejected solute atoms out of the precipitates. The shrinkage/dissolution phenomenon was detected when a precipitate in the pre-irradiation state shrinks in size post-irradiation, indicating the dissolution of solute atoms into the matrix. The growth/reprecipitation phenomenon was ascertained when a precipitate grows post-irradiation by acquiring solute atoms from the matrix. Figures 3 (b) and (d) also depict an inverse coarsening behavior [10], where relatively larger precipitates showed shrinkage/dissolution and smaller precipitates demonstrated growth/reprecipitation. Inverse coarsening refers to the growth of smaller precipitates at the expense of larger precipitates [10]. In the specifically selected regions of interest, a comparison between the 0.003 dpa and 0.3 dpa specimens indicates more instances of ballistic dissolution following 0.003 dpa irradiation, indicated by the red ellipses in Fig. 3 (b). Whereas the selected region of interest in the 0.3 dpa specimen shows more prevalence of nucleation and growth and growth/reprecipitation, indicated by the black and purple ellipses, respectively. The differences in the observations can be attributed to the fluence; in particular, the higher fluence and longer reactor residence time for 0.3 dpa irradiation, resulted in the prevalence of nucleation and growth, and the tendency towards inverse coarsening.

Figures 3 (e) - (h) show the selected regions of interest of the 3D μ-CT segmented tomographs demonstrating precipitate evolution phenomena that occurred post-annealing at 600 °C for up to 32 h. Precipitate evolution phenomena, such as nucleation and growth (black ellipses), shrinkage (orange ellipses), and growth (purple ellipses), occurred post-annealing. Similar to the irradiated specimens shown in Figs. 3 (a) - (d), the phenomena in the tomograph sections for pre-annealing and post-annealing studies were identified by monitoring individual precipitates and precipitate groups. In post-annealing specimens, smaller precipitates shrunk at the expense of the growth of larger precipitates, as shown in Figs. 3 (e) - (h), illustrating conventional coarsening behavior or Ostwald ripening that can be modeled by the mean-field theory of coarsening [23,24]. However, the coarsening effect observed post-annealing is in contrast with the inverse coarsening effect observed following neutron irradiation.

Precipitate Volume and Radii Evolution

Figures 4 (a) and (b) display a comparison of the precipitate volume distributions normalized by the volumes of the corresponding characterized HT-UPS steel specimens for pre-irradiation and post-irradiation of 0.003 dpa and 0.3 dpa at 600 °C, respectively. The 0.003 dpa specimen showed a reduction in the normalized counts of the precipitates in the volume range of 65 to 350 μm^3 as compared to the pre-irradiated specimen, illustrated in Fig. 4 (a). The largest overall maximum reduction in normalized precipitate counts was two orders of magnitude ranging from 1076 mm^{-3} to 84 mm^{-3}, observed for the precipitate volume range of 160 to 170 μm^3 following 0.003 dpa. However, an increase in the normalized precipitate count was observed below precipitate volumes of 65 μm^3. These results are summarized in Table 1, showing the arithmetic and lognormal means for precipitate volumes, along with the corresponding standard deviations. Following the 0.003 dpa irradiation, a reduction in the arithmetic (4.10 μm^3 to 3.01 μm^3) and lognormal means (3.17 μm^3 to 1.84 μm^3) occurred. Both reductions occurred within one standard deviation. However, the standard deviations for both means decreased after irradiation, particularly for the arithmetic mean, demonstrating a reduction in the range of precipitate volumes and a shift to smaller volumes. The decreasing trends in the precipitate volumes are the manifestations of the nucleation and growth, ballistic dissolution, and shrinkage/dissolution phenomena observed in Fig. 3 (b).

Similarly, in the 0.3 dpa specimen (Fig. 4 (b)), the precipitate count decreased in the volume range of 85 to 350 μm^3 and increased below a precipitate volume of 85 μm^3 as compared to pre-irradiation. However, the maximum reduction in normalized precipitate counts in the volume range of 85 to 350 μm^3 was only one order of magnitude lower as compared to the 0.003 dpa specimen, ranging from 203 mm^{-3} to 34 mm^{-3} for the precipitate volume range of 200 - 210 μm^3. A complete reduction in precipitate numbers with volumes greater than 240 μm^3 was observed following both irradiations. Arithmetic and lognormal means for precipitate volumes, along with corresponding standard deviations were calculated, as given in Table 1. Only slight changes in the arithmetic (8.84 μm^3 to 7.03 μm^3) and lognormal means (5.61 μm^3 to 5.60 μm^3) occurred after 0.3 dpa. Both reductions occurred within one standard deviation. The standard deviation for the arithmetic mean decreased, demonstrating a reduction in the range of precipitate volumes and a decrease in the precipitate volumes greater than 85 μm^3. However, the standard deviation for the lognormal mean increased. Since the larger precipitate volumes of a lognormal

distribution are weighted less, this highlights an increase in the number and range of smaller precipitates following the 0.3 dpa irradiation, therefore increasing the lognormal standard deviation. Although the normalized precipitate counts did not decrease as dramatically as the 0.003 dpa specimen for the smaller precipitates with volumes less than 350 μm^3 (Fig. 4 (b)), the reduction in the overall precipitate volumes still resulted in smaller means. The decreasing trends in the precipitate volumes are the result of the nucleation and growth, ballistic dissolution, and shrinkage/dissolution phenomena observed in Fig. 3 (d). Overall, neutron irradiation resulted in a reduction in arithmetic and lognormal mean precipitate volumes, despite the variations in the normalized volume distribution trends.

Figure 4 (c) displays a comparison of the precipitate volume distributions normalized by the characterized volumes of the corresponding HT-UPS steel specimen for pre-annealing and post-annealing at 600 °C for 3.2 h, 6.4 h, and 32 h. All precipitate volume ranges increased following annealing at 600 °C for 32 h, as compared to all other thermal treatments and the pre-annealed specimen. However, only minor precipitate volume changes were observed post-annealing after 3.2 h and 6.4 h, as compared to the pre-annealed specimen. Table 1 indicates this behavior quantitatively; the arithmetic and lognormal mean changes are within one standard deviation post-annealing for 3.2 h and 6.4 h. Whereas, post-annealing for 32 h increased the arithmetic (1.19 μm^3 to 11.26 μm^3) and lognormal means (1.69 μm^3 to 13.34 μm^3) of precipitate volumes by one order of magnitude compared to the pre-annealed condition. Figure 4 (d) demonstrates the nature of the precipitate distribution on the specimen surface of 0.3 dpa specimen, indicating the occurrence of both intragranular and intergranular precipitates.

Table 1 also shows the volume fraction (V_V) and surface area per unit volume (S_V) measurements of $Cr_{23}C_6$ precipitates for pre-irradiation and post-irradiation specimens (0.003 dpa and 0.3 dpa at 600 °C) and pre-annealing and post-annealing specimens (3.2 h, 6.4 h, and 32 h at 600 °C). A large reduction in V_V and S_V was observed following the 0.003 dpa irradiation, as compared to the pre-irradiation specimen. However, 0.3 dpa specimen indicated a nearly identical V_V and exhibited a small increase in S_V, as compared to the pre-irradiation specimen. An increase was observed in V_V and S_V, following annealing at 600 °C for 3.2 h and 6.4 h. However, further annealing up to 32 h resulted in the reduction of V_V and S_V.

Frequency distributions of the precipitate radii for pre-irradiation and post-irradiation of 0.003 dpa and 0.3 dpa at 600 °C are shown in Figs. 5 (a) and (b), respectively. Figures. 5 (a) and (b) indicate a similar behavior, as depicted in Figs. 4 (a) and (b), illustrating an increase in the frequency of smaller precipitates (<0.7 μm) and a decrease in the frequency of larger precipitates (> 0.7 μm) post-irradiation. These changes are also accompanied by a peak shift in the distribution to a lower value from 0.7 μm - 0.8 μm for pre-irradiation to 0.5 μm - 0.6 μm for both 0.003 dpa and 0.3 dpa irradiations.

The frequency distributions of the precipitate radii are shown in Fig. 5 (c) for pre-annealing and post-annealing at 600 °C for 3.2 h, 6.4 h, and 32 h. The peaks of the radii distributions increased from 0.5 μm - 0.6 μm for pre-annealing to 1.0 μm - 1.1 μm for post-annealing for 32 h. The breadth of the distribution increased, exhibited by the change in lognormal standard deviation, from 0.15 μm for the pre-annealing state to 0.66 μm for the post-annealed state after 32 h. Figure.

5 (c) illustrates a decrease in the frequencies of precipitate radii below 0.7 μm and an increase above 0.7 μm following annealing for 3.2 h and 6.4 h, as compared to pre-annealing. However, the lognormal mean radii exhibited negligible changes with values of 0.62 ± 0.15 μm pre-annealing, 0.64 ± 0.16 μm post-annealing for 3.2 h, and 0.63 ± 0.15 μm post-annealing for 6.4 h, whereas post-annealing for 32 h showed an increase in the lognormal mean radius to 1.30 ± 0.66 μm.

The growth law for coarsening behavior (Ostwald ripening) under annealing is modeled using the mean-field theory of coarsening (MFTC) and/or modified MFTC, which demonstrates that the change in arithmetic mean radii is directly proportional to $(\text{time})^{1/3}$ [23–25]. The evolution of the arithmetic mean radii following neutron exposure and thermal treatments were evaluated, as shown in Figure 6 to compare with the growth law. Figure 6 (a) shows the evolution of the arithmetic mean radii between pre-irradiation and post-irradiated states. Here, R_0 is the initial arithmetic mean radius, i.e., for pre-irradiation, and R is the arithmetic mean radius for post-irradiation states. Figure 6 (a) shows a reduction in the mean precipitate radius following irradiation of 0.003 dpa and 0.3 dpa, as compared to corresponding pre-irradiation states, which is also supported by the previously mentioned observations in Figs. 4 (a) and (b) and Figs. 5 (a) and (b). The decrease in the precipitate arithmetic mean radii is larger following the 0.3 dpa irradiation, as compared to the 0.003 dpa irradiation. This behavior is in qualitative agreement with nucleation and growth, ballistic dissolution, and shrinkage/dissolution phenomena observed in Figs. 3 (b) and (d).

The evolution of the arithmetic mean precipitate radii of the annealed precipitates is shown in Fig. 6 (b). Here, R_0 is the initial mean radius, i.e., for pre-annealing, and R is the mean radius for different annealing times. Figure 6 (b) shows an overall precipitate growth with post-annealing at 600 °C for 32 h, as compared to pre-irradiation, which is in agreement with the dominant coarsening behavior, including the growth of larger precipitates at the expense of smaller precipitates or Ostwald ripening, as depicted in Figs. 3 (e) and (h), and the trends observed in Fig. 4 (c) and Fig. 5 (c). However, Figure 6 (b) shows no changes in mean precipitate radii post-annealing for 3.2 h and 6.4 h, as compared to pre-irradiation, due to simultaneous nucleation and growth that compensate for the coarsening behavior, as shown Figs. 3 (e), (f), and (g).

The 0.003 dpa specimen and the post-annealing for 3.2 h specimen were subjected to nuclear reactor conditions and annealing conditions, respectively, for the same amounts of time. The evolution of mean precipitate radii comparison between the two conditions directly differentiates the irradiation and annealing effects. As shown in Fig. 6, the mean radius reduction following the 0.003 dpa irradiation indicates nucleation and growth, as well as ballistic dissolution phenomena, whereas a negligible change in mean the radius after 3.2 h annealing denotes the effects of the balance between nucleation and growth, as well as coarsening mechanisms.

Precipitate Sphericity Evolution

Figures 7 (a) - (d) show the precipitate volume and sphericity bivariate distributions for the pre-irradiated and post-irradiated HT-UPS steel specimens. Smaller precipitates with volumes less

than 100 μm^3 have the greatest number of large sphericities in the range of 0.9-1.1 for both the pre-irradiation and post-irradiation conditions, indicating smaller precipitates are more spherical. In the 0.003 dpa specimen, low sphericity (< 0.6) and large volume precipitates (100 – 350 μm^3) show a decrease in precipitate counts. This behavior coincides with an increased quantity of high sphericity (0.6 – 1.0) and precipitates in the range of 100 – 250 μm^3, as illustrated in Figs. 7 (a) and (b). This trend resulted in a minor increase of arithmetic mean sphericity of the precipitates from 0.93 ± 0.13 to 0.94 ± 0.11, as given in Table 1. The 0.3 dpa specimen demonstrated a decrease in the number of low sphericity (< 0.6) and large volume precipitates (100 – 350 μm^3), along with an increase in the number of high sphericity (0.6 – 1.0) precipitates in the range of 100 – 250 μm^3. Following the 0.3 dpa irradiation, the overall range of sphericity (0.45 – 1.2) is unchanged. However, a shift in sphericity range is observed following the 0.003 dpa irradiation from 0.3 to 1.2 for the pre-irradiated specimen to 0.45 to 1.2 post-irradiation, indicating a tendency towards more spherical precipitates post-irradiation. Table 1 also indicates no change in the arithmetic mean sphericities following 0.3 dpa irradiation (0.94 ± 0.11) compared to pre-irradiation (0.94±0.12).

Figures 7 (e) - (h) represent the precipitate sphericity and volume bivariate distributions of the HT-UPS steel specimens for pre-annealing and post-annealing at 600 °C for 3.2 h, 6.4 h, and 32 h. Similar to pre-irradiation and post-irradiation specimens, precipitates with volumes less than 100 μm^3 have the greatest numbers of higher sphericities in the range of 0.9-1.1 for both the pre-annealing and post-annealing conditions, indicating that smaller precipitates are more spherical. Figures 7 (e) and (h) illustrate an increase in precipitate numbers with volumes greater than 300 μm^3 with lower sphericity (<0.6) along with a reduction in relatively smaller precipitates (<200 μm^3) with peak sphericities of 0.9-1.0, following post-annealing at 600 °C for 32 h. These observations agree with the small decrease observed in the arithmetic mean sphericity from 0.95 ± 0.11 to 0.93 ± 0.11, as demonstrated in Table 1, as compared to pre-annealing. Post-annealing at 600 °C for 3.2 h and 6.4 h showed a decrease in the counts of smaller precipitates (<100 μm^3) with peak sphericities of 0.9 – 1.1 with a simultaneous increase in relatively larger precipitates (<200 μm^3) with lower sphericities (<0.6) in comparison to pre-annealing, as illustrated in Figs. 7 (e), (f), and (g). However, the arithmetic mean precipitate radii did not change following 3.2 h and 6.4 h annealing, as shown in Table 1, due to the compensation in the reduction of precipitate numbers with higher sphericities (0.9 - 1.1) and an increase in precipitate numbers with lower sphericities (<0.6).

Discussion

Neutron Irradiation Effects on $Cr_{23}C_6$ Evolution

In the recent XANES study conducted by Nori et al. [15], using the identical irradiated HT-UPS steel specimens, $Cr_{23}C_6$ concentration generally increased with irradiation, indicating the possibility of concurrent evolution phenomena, including nucleation and growth, ballistic dissolution, and inverse coarsening (including growth/reprecipitation, as well as shrinkage/dissolution) [15]. However, XANES is unable to discern morphological characteristics or quantities of precipitates, thus µ-CT was utilized to characterize the neutron irradiated

specimens before and after irradiation. The current study confirms the co-existence of these phenomena and corroborates the XANES study [15], establishing an early onset of $Cr_{23}C_6$ precipitate evolution. Moreover, the presence of $Cr_{23}C_6$ precipitates pre-irradiation and their mechanistic evolution in the form of nucleation and growth, ballistic dissolution, shrinkage/dissolution, and growth/reprecipitation post-irradiation support that these phases are radiation enhanced.

Previous studies have suggested that $M_{23}C_6$ is a radiation-enhanced phase above 550 °C in austenitic stainless steels since limited $M_{23}C_6$ formation occurs with thermal aging in the range of 550 °C – 900 °C [26–28]. For example, this behavior was illustrated with an alloy similar to HT-UPS steel, a Ti-stabilized 15% Ni, 15% Cr steel with the presence of intergranular $M_{23}C_6$ following 1.5 dpa neutron irradiation at 577 ± 25 °C [28]. However, the same study indicated that $M_{23}C_6$ had limited existence after aging in similar conditions [28]. Neutron irradiation (36 dpa at 600 °C to 630 °C) of 20% cold-worked (CW) Ti-stabilized 316 stainless steel showed inter-granular formation of $M_{23}C_6$ [22]. While neutron irradiation of FV548 (~ 16% Cr, ~ 12% Ni) Nb-stabilized steel indicated the formation of both intra-granular and inter-granular $M_{23}C_6$ following 16 dpa at 475 °C to 600 °C for 20% CW specimens and at 550 °C to 700 °C for solution annealed materials [29]. Moreover, stable nucleation and growth of $M_{23}C_6$ in 304 stainless steels were predicted by rate theory models to occur in the range of 550 °C and 650 °C for a maximum sink density of 10^{13} m^{-2} and a minimum point-defect generation rate of 10^{-8} dpa/s [30,31]. Hence, previous neutron irradiation studies indicated the stable formation of $M_{23}C_6$ in austenitic stainless steels at temperatures above 550 °C. However, the neutron fluences (from 0.003 dpa to 0.3 dpa) in the current research and the XANES study [15], are one or more orders of magnitude lower compared to previous studies (1.5 dpa) which defined $M_{23}C_6$ as a radiation-enhanced phase [28].

The current research characterized the spatial distribution and the morphological evolution of $Cr_{23}C_6$ precipitates as a function of neutron irradiation dose. For example, the 0.003 dpa specimen demonstrated a reduction of two orders of magnitude in the normalized precipitate count for larger precipitates (ranging from 65 to 350 μm^3), shown in Fig. 4 (a), as compared to the pre-irradiated specimen. This behavior is less pronounced in the 0.3 dpa specimen showing only one order of magnitude reduction (Fig. 4(b)) in the precipitate count for the larger precipitates (85 to 350 μm^3) compared to the pre-irradiated specimen. Figures 5 (a) and (b) indicate a shift in precipitate radii distributions to smaller sizes (0.5-0.6 μm) following irradiation in comparison to the pre-irradiation values of 0.7-0.8 μm. Thus, the irradiation of the samples creates smaller precipitates while reducing the overall quantity of larger precipitates. This behavior is also captured by the reduction of the post-irradiated mean precipitate volumes, as expressed in Table 1, and the decrease of the mean precipitate radii following irradiation, shown in Figs. 5 (a) and (b). These observations are the manifestations of the numerous precipitate evolution mechanisms observed in the regions of interest in the HT-UPS steel specimens, as depicted in Figs. 3 (a) - (d). Thus, irradiation-induced precipitate nucleation and growth, as well as ballistic dissolution phenomena, become active and contribute to the reduction in precipitate sizes following neutron irradiation.

As previously mentioned, the 0.003 dpa specimens exhibited a greater reduction in precipitate counts for the volume range of 65 to 350 μm^3 versus precipitates ranging in volume from 85 to 350 μm^3 for the 0.3 dpa specimen, as depicted in Fig. 4 (a) and (b). This discrepancy may be attributed to the favorable kinetics (e.g., longer reactor residence time) provided during

0.3 dpa fluence to facilitate additional inverse coarsening behavior in the form of growth/reprecipitation of the smaller precipitates (<85 μm^3), shown in Fig. 3 (d). Although more instances of growth/reprecipitation of the smaller precipitates occur in 0.3 dpa specimen, the dominance of nucleation and growth, as well as ballistic dissolution phenomena, observed in 0.3 dpa specimen manifest in an overall reduction of the arithmetic mean precipitate radii compared to 0.003 dpa, as illustrated in Fig. 6 (a).

Nucleation and growth of precipitates can be attributed to radiation-enhanced diffusion of point defects leading to solute supersaturation [10]. Moreover, the excess point defects, particularly vacancies [16,22], can be bound to relatively bigger size solute atoms, such as Cr [10], and facilitate the nucleation of $Cr_{23}C_6$ precipitate phases. Thus, the accumulation of vacancies can lead to void-associated precipitates post-irradiation, as observed in neutron-irradiated austenitic stainless steels [22,32]. Additionally, HT-UPS steel generally exhibits annealing twin boundaries [33], which can also act as sites for the nucleation of precipitate phases of type $M_{23}C_6$ [11]. Pre-existing TiC precipitates [34] and dislocation loops [35] can also act as $M_{23}C_6$ nucleation sites. Ballistic dissolution of the precipitates can be attributed to the cascades during irradiation, which can cause solute atom displacement [10,36]. Thus, ballistic effects can lead to precipitate dissolution during irradiation, as shown in Fig. 3 (red ellipses).

Differentiation of Neutron Irradiation Effects from Annealing Effects on $Cr_{23}C_6$ Evolution

The dominance of coarsening behavior in annealed specimens is indicated by the increase in normalized precipitate counts for all volume ranges (Fig. 4 (c)), as well as the peak shift in the frequency distributions for radii from 0.5 - 0.6 μm (pre-annealing) to 1.0 - 1.1 μm (post-annealing at 32 h) (Fig. 5 (c)). These observations are the manifestations of shrinkage and growth phenomena illustrated in Figs. 3 (e) – (h). The prevalence of coarsening behavior is expected during annealing according to Ostwald ripening [23,24], in which larger precipitates (> 1 μm) grow at the expense of smaller precipitates. For example, in steels similar to HT-UPS steels, such as Ti modified austenitic stainless steels, coarsening of $M_{23}C_6$ precipitates was observed after aging at temperatures above 600 °C [22,37].

However, in addition to coarsening, precipitate nucleation and growth were also observed, particularly post-annealing for 3.2 h and 6.4 h, as shown in Figs. 3 (f) and (g). Previous experimental studies indicated nucleation and growth of $M_{23}C_6$ precipitates in austenitic stainless steels annealed at temperatures > 550 °C at various nucleation sites, including grain boundaries, twin boundaries, and dislocations [38–42]. Simulation studies also used various models that included simultaneous nucleation, growth, and coarsening behaviors to obtain the evolution characteristics of $M_{23}C_6$ precipitates comparable to experimental studies, as well as at longer aging times [8,43]. For example, a theoretical study of HT-UPS steel utilized classical nucleation theory and thermodynamic extremum principles to reveal the formation of stable $M_{23}C_6$ precipitates, greater than 100 nm in size, following aging at 700 °C for 100,000 h [8]. It was found that nucleation and growth of $M_{23}C_6$ precipitates occurred in the early stages of annealing (<3 h) [8,43]. The same study also demonstrated an increase in the $Cr_{23}C_6$ phase fraction from 0 to a maximum

of ~ 0.004 after 3 h of annealing at 700°C. The phase fraction gradually decreased to nearly zero after 10,000 hours, demonstrating precipitate dissolution into the matrix [8]. In 316H stainless steel (17.17% Cr, 11.83% Ni), the number density of $Cr_{23}C_6$ precipitates increased from zero to ~ $1.7x10^{19}$ mm^{-3} after annealing at 700 °C for ~ 0.3 h, remained constant until ~ 3 h, and then decreased gradually after 3 h, showing the dissolution of the precipitates into the matrix [43]. In the current research, nucleation and growth phenomena are observed in the early stages of annealing at 600 °C for 3.2 h and 6.4 h, as shown in Figs. 3 (f) and (g). Whereas after 32 h of annealing at 600 ºC, precipitate growth was more evident, as evidenced by Figs. 3 (h) and 4 (c).

The evolution of mean radii of the precipitates shown in Fig. 6 (b), did not clearly indicate a linear trend, indicative of a constant coarsening rate, as expected with Ostwald ripening, and as modeled by MFTC. Since the MFTC model assumes diffusion-limited coarsening, a spherically symmetric field of diffusion, and a constant mean concentration far from the precipitates [23–25], any deviations from the assumptions can cause a discrepancy in the expected linear trend. However, the discrepancies observed in this study can be primarily attributed to the simultaneous nucleation and/or growth of precipitates during annealing, particularly for 3.2 h and 6.4 h, along with concurrent coarsening behavior. Thus, mean radii did not deviate after 3.2 h and 6.4 h annealing times due to the compensation of coarsening by nucleation and growth of $Cr_{23}C_6$ precipitates, as shown in Fig. 6 (b). However, at longer annealing times (e.g., 32 h), coarsening behavior dominated, as shown in Fig. 3 (h), and hence, there is a possibility for a linear mean radii evolution trend for annealing times greater than 6.4 h, representing a constant coarsening rate. Also, precipitates with a radius less than 0.46 µm for the pre-annealed, 3.2 h, and 6.4 h annealed specimens, and precipitates with a radius less than 0.91 µm for the 32 h annealed specimen, were below the resolution limit of the technique, therefore obscuring any nucleation and growth for very small precipitates. Thus, the effects of annealing were differentiated from the irradiation conditions since the irradiation studies showed a dominant tendency of precipitate nucleation and/or growth, ballistic dissolution, and inverse coarsening.

As shown in Table 1, the 0.003 dpa specimen demonstrated a reduction in both V_V and S_V; whereas the 0.3 dpa specimen demonstrated a nearly identical V_V and an increase in S_V, as compared to corresponding pre-irradiation specimens. Previous XANES studies [15] illustrated an increase in spectral density with irradiation, which agrees with the increase in S_V and little change in V_v following the 0.3 dpa irradiation. However, the XANES trend of increasing spectral density is not consistent with the results observed in the current study for the 0.003 dpa specimen, which could be attributed to various technique limitations for both XANES and µ-CT. The current study indicated that the dominant mechanisms controlling precipitate behavior in the 0.003 dpa specimen were ballistic dissolution, and nucleation and growth. This was also supported by the decrease in the average precipitate radii and volume. Thus, decreasing trends in size may lead to precipitate sizes that are below the detectable thresholds of the µ-CT technique. Moreover, the XANES studies were conducted on a smaller volume since it is a surface-based technique compared to the µ-CT studies. This may be exacerbated by an inhomogeneous distribution of $Cr_{23}C_6$ precipitates forming networks at the grain boundaries, albeit intra-granular precipitates were also identified in Fig. 4 (d).

As shown in Table 1, V_V and S_V increased following annealing at 600 °C up to 6.4 h, and then decreased for the remainder of the annealing time of 32 h. These changes are consistent with previous studies [8,43], which demonstrated a maximum precipitate phase fraction after ~ 3 h of annealing and then gradually decreased with further annealing at 700 °C. In the current study, the annealing temperature (600 °C) is less than the previous studies (700 °C) and hence, the annealing time for achieving a maximum V_V shifted from ~ 3 h for the previous studies to beyond 3.2 h in the current study.

The sphericity distribution changes following irradiation demonstrated different trends. The 0.003 dpa specimen showed an increase in the arithmetic mean sphericity, as expressed in Table 1, as compared to pre-irradiation. The increase in mean sphericity was accompanied by a concurrent reduction in the number of precipitates within the volume range of 100 – 350 μm^3 and lower sphericity (< 0.6) and an increase in the number of precipitates with volumes ranging from 100 – 250 μm^3 possessing higher sphericities (0.6 – 1.0), as illustrated in Figs. 7 (a) and (b), following irradiation. These trends can be the manifestations of ballistic dissolution and/or shrinkage/dissolution of larger precipitates, as well as the nucleation and growth of relatively smaller precipitates. However, Figs. 3 (a) and (b) depict the dominance of ballistic dissolution phenomenon resulting in the dispersion of larger volume and lower sphericity precipitates, as compared to the relatively smaller size and higher sphericity $Cr_{23}C_6$ precipitates.

The 0.3 dpa specimen showed no change in arithmetic mean sphericity, given in Table 1, as compared to pre-irradiation. This was accompanied by a reduction in the number of large volume precipitates (100 – 350 μm^3) and an increase in the number of precipitates ranging from 100 – 250 μm^3 with high sphericities (0.6 – 1.0), as illustrated in Figs. 7 (c) and (d). However, after 0.3 dpa irradiation, the sphericity range remained identical (0.45 – 1.2). These trends can be attributed to the prevalence of reprecipitation/growth due to inverse coarsening in the 0.3 dpa specimen, as shown in Fig. 3 (d). Thus, the increase in sphericity caused by ballistic dissolution is balanced by a decrease in sphericity caused by reprecipitation/growth of precipitates following 0.3 dpa irradiation.

The post-annealing at 600 °C for 32 h specimen indicated a decrease in arithmetic mean sphericity, as demonstrated in Table 1, as compared to the pre-annealing specimen. This was accompanied by an increase in the number of precipitates with volumes greater than 300 μm^3 with lower sphericity (<0.6), and a simultaneous reduction in the number of precipitates less than 200 μm^3 with peak sphericities of 0.9-1.0, as illustrated in Figs. 7 (e) and (h). This is a result of coarsening behavior observed in Fig. 3 (h), in which larger $Cr_{23}C_6$ precipitates with lower sphericities grow at the expense of smaller precipitates with higher sphericities. The morphological trends in this study are in agreement with previous studies in austenitic stainless steels which confirmed that larger precipitates possessed lower sphericity geometries, such as rods or plates, which were generally inter-granular in nature, whereas smaller precipitates tended to be located intra-granularly with higher sphericity shapes, such as cuboids or octahedrons following post-irradiation [34,44] and post-annealing [38–42] characterization.

Previous studies depicted the formation of $Cr_{23}C_6$ precipitates both at grain boundaries [6,22,28,29] and within the grains [22,32,34,35]. The variation in precipitate localities can be

advantageous to impart radiation resistance due to the ability to effectively annihilate point defects in the matrix and at interfaces, such as grain boundaries and twin boundaries. This advantage is further supplemented by the inhibition of grain boundary embrittlement by inter-granular precipitates [45]. In the current investigation, $Cr_{23}C_6$ precipitates were dispersed throughout the specimens, demonstrating inter-granular and intra-granular locations, as illustrated in Fig. 4 (d), thus supporting the propensity for enhanced radiation resistance in HT-UPS steels.

Conclusions

Four-dimensional precipitate evolution in HT-UPS steel subjected to irradiation or annealing was obtained by conducting synchrotron X-ray propagation-based phase-contrast enhanced µ-CT on identical specimens. A multi-step model-based segmentation technique was designed to segment low volume fractions of second phase particles in images with substantial noise, which allowed for individual precipitate characteristics to be analyzed, including volume, surface area, radius, sphericity, V_V, S_V, and grain locality. This analysis also provided insight into the phenomena or mechanisms responsible for the specific precipitate evolution such as nucleation and growth, ballistic dissolution, shrinkage/dissolution, and growth/reprecipitation.

Neutron irradiation of 0.003 dpa and 0.3 dpa at 600 °C resulted in various $Cr_{23}C_6$ precipitate evolution phenomena such as nucleation and growth, ballistic dissolution, and inverse coarsening, including shrinkage/dissolution of precipitate radii > 0.7 µm and growth/reprecipitation of precipitate radii <0.7 µm. Simultaneously, neutron irradiated specimens demonstrated a reduction in $Cr_{23}C_6$ precipitate volume distributions for larger precipitates (65- 350 μm^3 for 0.003 dpa and 85- 350 μm^3 for 0.3 dpa). Also, a peak shift in radii frequency of $Cr_{23}C_6$ precipitates was observed from 0.7 - 0.8 to 0.5 - 0.6 as compared to pre-irradiation. These trends indicate the dominance of nucleation and growth, as well as and ballistic dissolution phenomena for the irradiated specimens. Following 0.3 dpa neutron exposure, both inter-granular and intra-granular precipitates still existed, indicating the desired radiation resistant response to enable effective point defect and He trapping in multiple localities, as well as mitigating dislocation movement. The sphericity evolution of the $Cr_{23}C_6$ precipitates in the 0.003 dpa specimen indicated a simultaneous precipitate number reduction for volumes ranging from 100 – 350 μm^3 with lower sphericities (< 0.6) and a precipitate number increase for volumes ranging from 100 – 250 μm^3 with higher sphericities (0.6 – 1.0), primarily due to ballistic dissolution. The sphericity evolution of $Cr_{23}C_6$ precipitates in the 0.3 dpa specimen demonstrated a precipitate number reduction in the volume range from 100 – 350 μm^3 for sphericities <0.6 and an increase in the precipitate numbers within the volume range of 100 – 250 μm^3 for sphericities ranging from 0.6 to 1.0, due to the equilibrium between ballistic dissolution and reprecipitation/growth phenomena.

In comparison, nucleation and growth, shrinkage, and growth were observed following annealing at 600 °C for up to 32 h. The dominance of coarsening behavior, including the growth of larger particles at expense of smaller precipitates (Ostwald ripening) was observed in annealed specimens, indicated by the increase in normalized precipitate counts for all volume ranges and the peak shift in the frequency distributions for radii ranging from 0.5 - 0.6 µm (pre-annealing) to 1.0 - 1.1 µm (post-annealing at 32 h). The sphericity evolution of the $Cr_{23}C_6$ precipitates following annealing at 600 °C for 32 h indicated an increase in the number of precipitates with volumes

larger than 300 μm^3 and lower sphericity (<0.6), along with a simultaneous reduction in relatively smaller precipitates (<200 μm^3) with peak sphericities of 0.9-1.0, due to the coarsening behavior.

The current research elucidated geometrical precipitate evolution trends, as a function of irradiation or annealing, and the corresponding mechanism(s) responsible for the evolution. The 4D geometrical and phenomenological results reported can be used to parameterize and validate mesoscale models, as well as to potentially tailor a desired microstructure using neutron radiation or thermal processes.

Materials and Methods

The HT-UPS steel was fabricated at Oak Ridge National Laboratory (ORNL) with the chemical composition described in Table 2. Parallelepiped specimens of HT-UPS steel with dimensions ~ 0.5 x ~ 0.5 x 5-7 mm were fabricated for this study. Neutron irradiations and annealing treatments were performed separately on specimens, as described in 44Table 3. Each specimen was uniquely characterized via synchrotron µ-CT before and after undergoing irradiation or annealing to capture the evolution of the individual precipitates. Neutron irradiations were performed in the High Flux Isotope Reactor at ORNL on two specimens to fluences of 0.003 dpa and 0.3 dpa corresponding to 3.2 h and 320 h at 600 °C in reactor, respectively. A description of an analogous irradiation device is found in McDuffee et al. [46]. The heat treatment experiment was performed on one specimen annealed at 600ºC for a total of 3.2 h, 6.4 h, and 32 h. The 3.2 h anneal corresponds with the reactor residence time for the 0.03 dpa specimen. Each annealing step was followed by synchrotron µ-CT imaging. Annealing cycles were carried out at 32 °C/min during heating and 110 °C/min during cooling.

Synchrotron µ-CT imaging was performed at the Advanced Photon Source (APS) beamline 1-ID-E at Argonne National Laboratory. A comprehensive description of the beamline for analogous µ-CT measurements is given in Thomas et al. [18] and Hunter et al. [47]. The beam was attenuated by the sample and then captured by a QImaging Retiga or Point Gray Grasshopper3 camera with an objective lens (x 10 or x 5) looking at a turning mirror to a 25 µm thick lutetium scintillator. Propagation-based phase-contrast enhanced tomography [18] was utilized with a sample to detector distance ranging from 50-70 mm. The pixel pitch is calculated from the camera sensor pixel pitch and the objective lens and verified through known distance measurements. The pixel pitch values are given in Table 3 for each experiment. Each specimen was imaged using a monochromatic X-ray parallel beam while rotating the specimen from 0° to 360°. The radiographs were converted to attenuation projections using the Beer-Lambert law and the light and dark images [48]. The cross-sectional images of the sample were reconstructed using the RECON software [49] via a filtered parallel back-projection method [50]. The resulting tomograph is a 3D representation of the local attenuation encoded into discrete 32-bit voxels in mm^{-1} stored as an image stack, with slices perpendicular to the X-ray direction (z-direction).

To analyze the precipitate volume, size, and geometry, it is necessary to segment the precipitates from the Fe-Cr-Ni matrix of HT-UPS steel, using model-based segmentation. Most images can be modeled as a Gaussian random process. This construction is the basis for many

classical segmentation techniques, such as global thresholding, stem from as they try to separate two distinct Gaussian processes from each other [51,52]. The simplest and most widely utilized global threshold segmentation is ineffective in this study due to the small volume percent of the second-phase precipitates (<1 volume %), which causes the attenuation distribution of the matrix to overshadow that of the precipitates [51], thus producing a large quantity of false-positive classifications from the matrix. The main limitation of the Gaussian construction of images is the existence of edges between features, which are the focus of the model-based segmentation technique presented in this study. Propagation-based phase-contrast radiographs rather than classical absorption radiographs (taken at closest approach of the sample to detector distance) are utilized to capitalize on the edge behavior to aid in segmentation. This technique reveals finer detail in the boundaries between objects from the modulated intensity patterns caused by the phase shifts in the X-ray as it passes through a boundary [53,54]. The current study utilizes the Sobel edge filter [20] to identify potential features. This is followed by the iterative active contour algorithm, which verifies the features and establishes boundaries utilizing a non-local mean schema [21].

The sample background edge was identified utilizing the Sobel edge filter on the entire image. The sample background edge image is then inputted into the Chan-Vese iterative area contour algorithm [21] to separate the background from the sample. The results were eroded to remove streaking artifacts from specimen edges, the boundary edges of the specimen, and the background before further image processing.

To segment the precipitates from the matrix, a Sobel edge filter [20] was also applied, excluding the background, sequentially in the z-direction to the tomographs to obtain input for the Chan-Vese algorithm [21]. The Chan-Vese algorithm was applied sequentially in the z-direction with a maximum of 300 iterations to produce a binary 3D segmentation image. Gaussian random numbers with mean and variance derived from the maximum likelihood estimate of the specimen were assigned to background voxels to avoid bias from the background.

After the segmentation, the total precipitate volume was determined by separation into individual precipitates using a 26-voxel neighborhood classification algorithm. The volume of each precipitate was calculated by counting the voxels that constituted the individual object and converted into μm using the pixel pitch. Precipitates with volumes of less than two voxels were excluded in the volume distributions due to the theoretical resolution of the system. To investigate precipitate evolution trends, the precipitate volume distributions were normalized based on the specimen volume analyzed. The average or arithmetic mean of the precipitate volume was calculated by taking the sum of all the precipitate volumes, x_i, divided by the number of all precipitates, N, given by $\sum x_i/N$. The standard deviation of the average was calculated using $\sqrt{\sum(x_i-\mu)^2/N}$. The lognormal statistics of the precipitate volume were calculated by taking the natural logarithm of the volume of each precipitate, x_i, followed by calculating the average, $\mu = \sum ln(x_i)/N$, and the standard deviation, $\sigma = \sqrt{\sum(ln(x_i)-\mu)^2/N}$, of the log values. The lognormal mean was then calculated using $e^{\mu+\sigma^2/2}$, while the lognormal standard deviation was calculated using $\sqrt{e^{(2\mu+\sigma^2)}(e^{\sigma^2}-1)}$. To further quantify evolution trends, volumetric measurements were converted to equivalent sphere radii (referred to as radii). The precipitate radii

frequency distributions were calculated by taking the number of precipitates in a bin and dividing by both the total amount of precipitates in the sample and the total volume of the sample.

The surface area was calculated with the adapted Crofton algorithm [55]. Traditionally, the surface area has been calculated in a 3D discrete body by utilizing the marching cubes method [56]. The marching cubes algorithm reconstructs an object from a 3D body utilizing weighted sub-voxel triangles [56] to estimate surface area. As the surface is reconstructed utilizing triangles rather than rounded edges, it overestimates the surface area. It is typically assumed that a sphericity value of greater than 0.6 is perfectly spherical when using the marching cubes method [57,58]. The adaptation of the Crofton method [55] does this differently by instead using the Crofton formula to express perimeter and area utilizing intersections of discrete lines onto a unit sphere projection [55]. This approach enables using a unit sphere projection rather than a triangular projection. By utilizing the Crofton method for surface area, a more accurate interpretation of surface area can be obtained without a positive bias in surface area, which is prevalent in the marching cubes method [55,56]. The adapted Crofton algorithm results in a perfectly spherical object with a sphericity of 1.0. The sphericity of each precipitate was then calculated utilizing the volume of the object and the surface area to quantify morphological changes. Each sample was analyzed utilizing the procedure described, and distributions of volume and sphericity were calculated.

Precipitates with volumes less than six voxels were not included in the sphericity distribution due to limitations of the adapted Crofton algorithm [55]. The V_V of each specimen was calculated by taking the total volume of the segmented precipitates and dividing it by the total volume of the specimen. The S_V of each specimen was calculated by taking the total surface area of all the precipitates and dividing it by the total volume of the specimen.

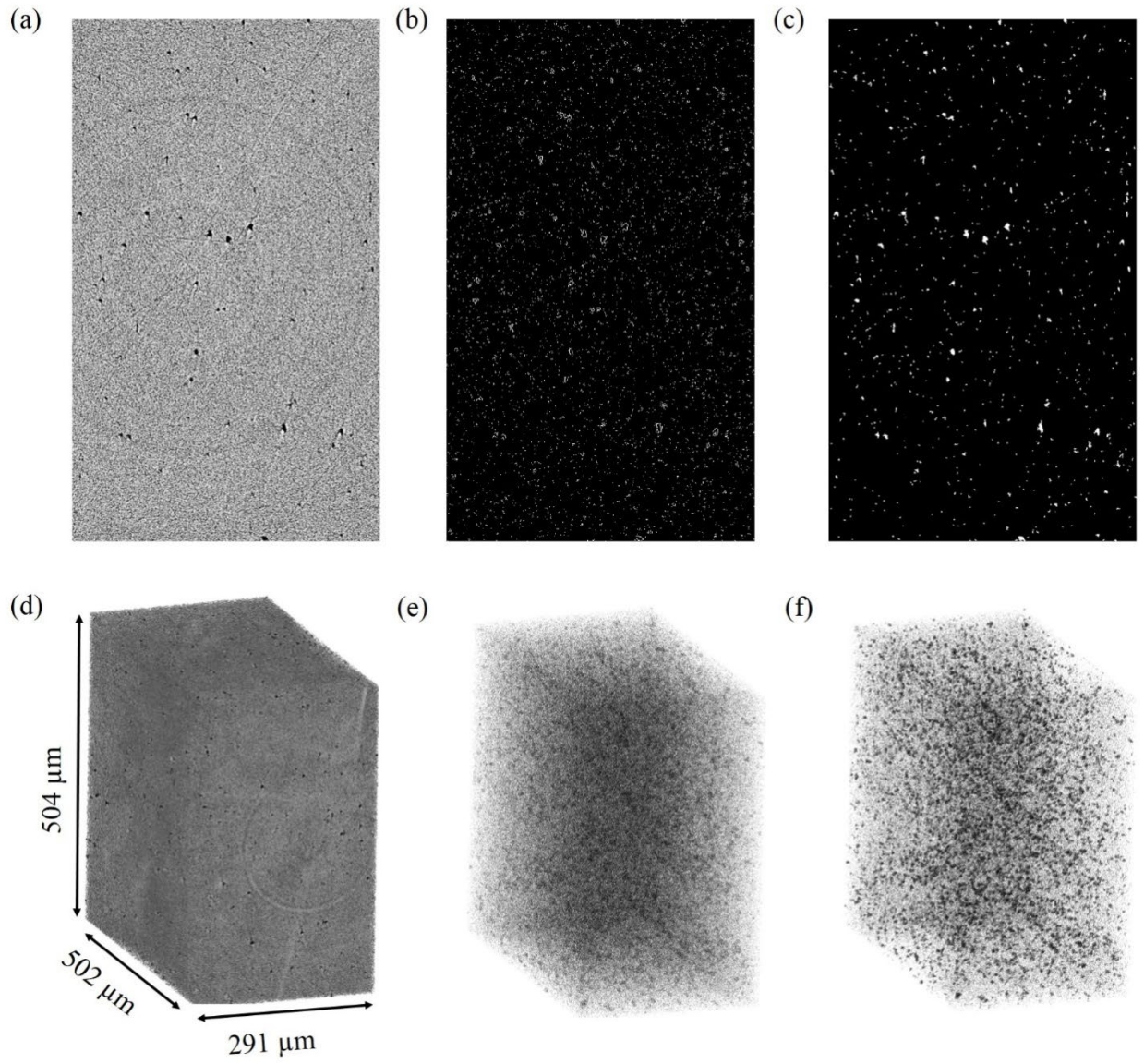

Figure 1. Sequential illustration of the precipitate segmentation procedure in HT-UPS steel using synchrotron µ-CT images. (a) A representative tomography slice of the pre-annealed specimen. The gray value represents the attenuation coefficient of the material. (b) The same slice shown in (a) after the application of the Sobel edge filter where the white regions represent the segmented edges. (c) Binary image output obtained using edge input into an iterative area-contour Chan-Vese segmentation algorithm. White regions correspond to the segmented precipitates. Figures 1 (d), (e), and (f) illustrate the 3D representations of the specimen corresponding to the 2D tomography slices shown in (a), (b), and (c), respectively.

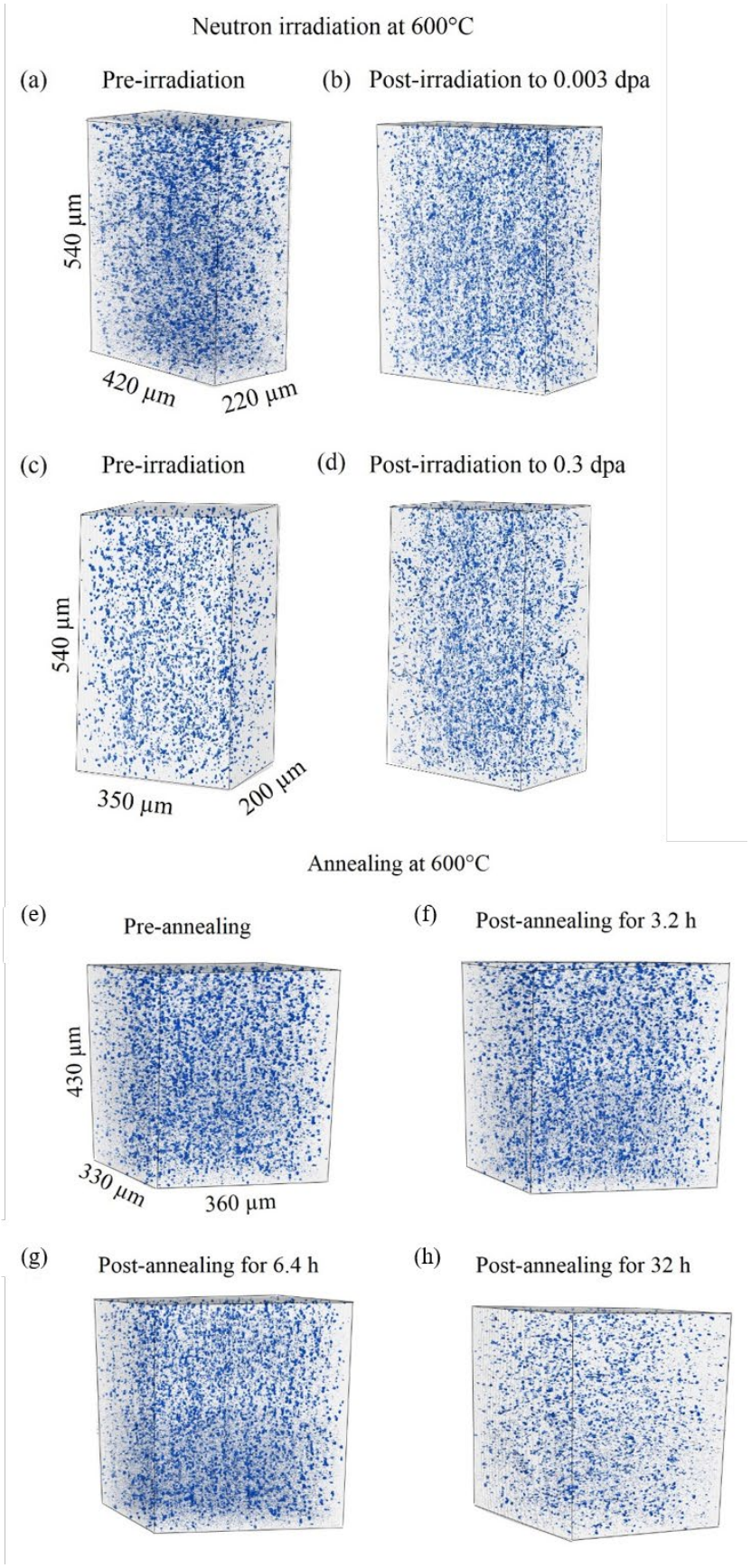
Neutron irradiation at 600°C
(a) Pre-irradiation
(b) Post-irradiation to 0.003 dpa
540 µm
420 µm
220 µm
(c) Pre-irradiation
(d) Post-irradiation to 0.3 dpa
540 µm
350 µm
200 µm
Annealing at 600°C
(e) Pre-annealing
(f) Post-annealing for 3.2 h
430 µm
330 µm
360 µm
(g) Post-annealing for 6.4 h
(h) Post-annealing for 32 h

Figure 2. Three-dimensional segmentation of precipitate isosurfaces, represented as blue features, obtained using μ-CT depicting the evolution of precipitates in HT-UPS steel for (a) pre-irradiation for 0.003 dpa and (b) post-irradiation to 0.003 dpa at 600 °C, (c) pre-irradiation for 0.3 dpa and (d) post-irradiation to 0.3 dpa at 600°C, (e) pre-annealing, (f) post-annealing at 600 °C for 3.2 h, (g) post-annealing at 600 °C for 6.4 h (h), and post-annealing at 600 °C for 32 h. The outlines indicate the boundaries of the cropped regions of the analyzed sample volumes.

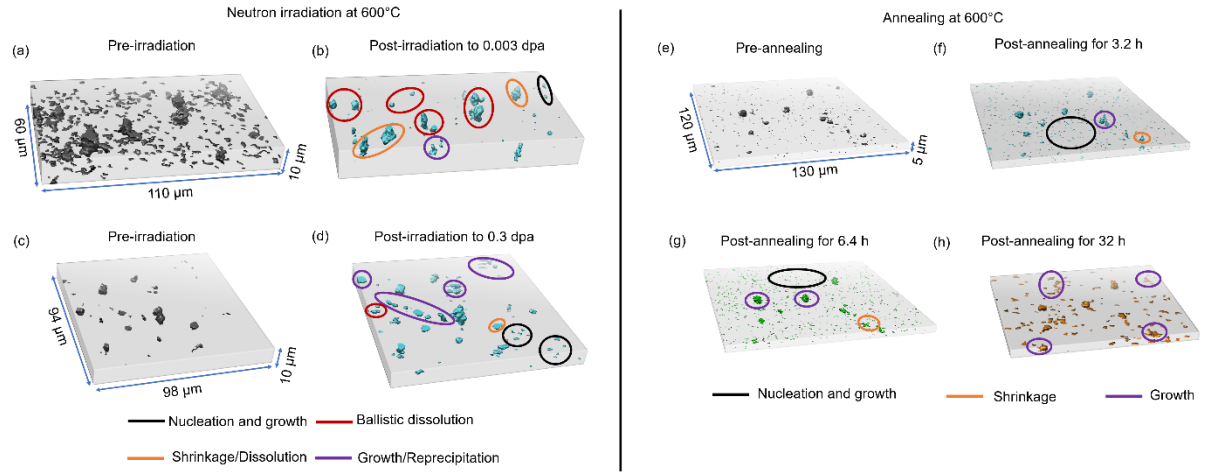

Figure 3. Precipitate evolution phenomena in HT-UPS steel in selected specimen regions as a function of irradiation at 600 °C for (a) pre-irradiation for 0.003 dpa, (b) post-irradiation to 0.003 dpa, (c) pre-irradiation for 0.3 dpa, and (d) post-irradiation to 0.3 dpa. Precipitate evolution phenomena in selected specimen regions as a function of annealing at 600 °C for (e) pre-annealing, (f) post-annealing for 3.2 h, (g) post-annealing for 6.4 h, and (h) post-annealing for 32 h. Isosurfaces of the segmented precipitates are illustrated within the selected regions of the samples. Marked instances of irradiation-induced precipitate evolution phenomena including nucleation and growth, ballistic dissolution, shrinkage/dissolution, and growth/reprecipitation are indicated. For the annealed samples, instances of nucleation and growth, shrinkage, and growth are indicated.

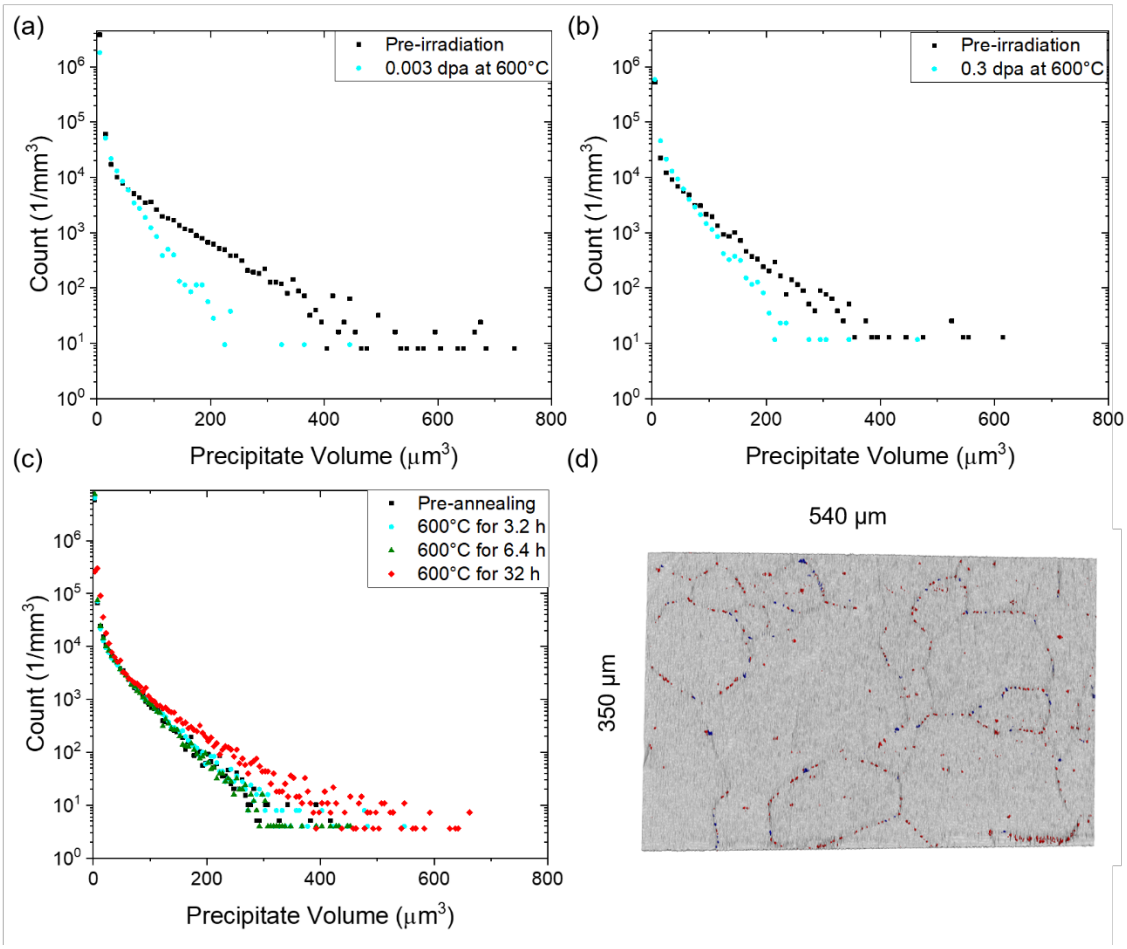

Figure 4. Precipitate volumes of the in HT-UPS steel samples normalized by the specimen volume characterized for: (a) pre-irradiation and post-irradiation of 0.003 dpa at 600°C, (b) pre-irradiation and post-irradiation of 0.3 dpa at 600 °C, and (c) pre-annealing and post-annealing at 600 °C for 3.2 h, 6.4 h, and 32 h. Each point represents the center of a precipitate volume bin of 10 μm^3. (d) A representative example of the surface of an HT-UPS steel tomograph indicating precipitate distribution in the 0.3 dpa specimen demonstrating the presence of both intergranular and intragranular precipitates. The red color indicates precipitates in volume $\leq$50 μm^3, while the blue color indicates precipitates in volume > 50 μm^3.

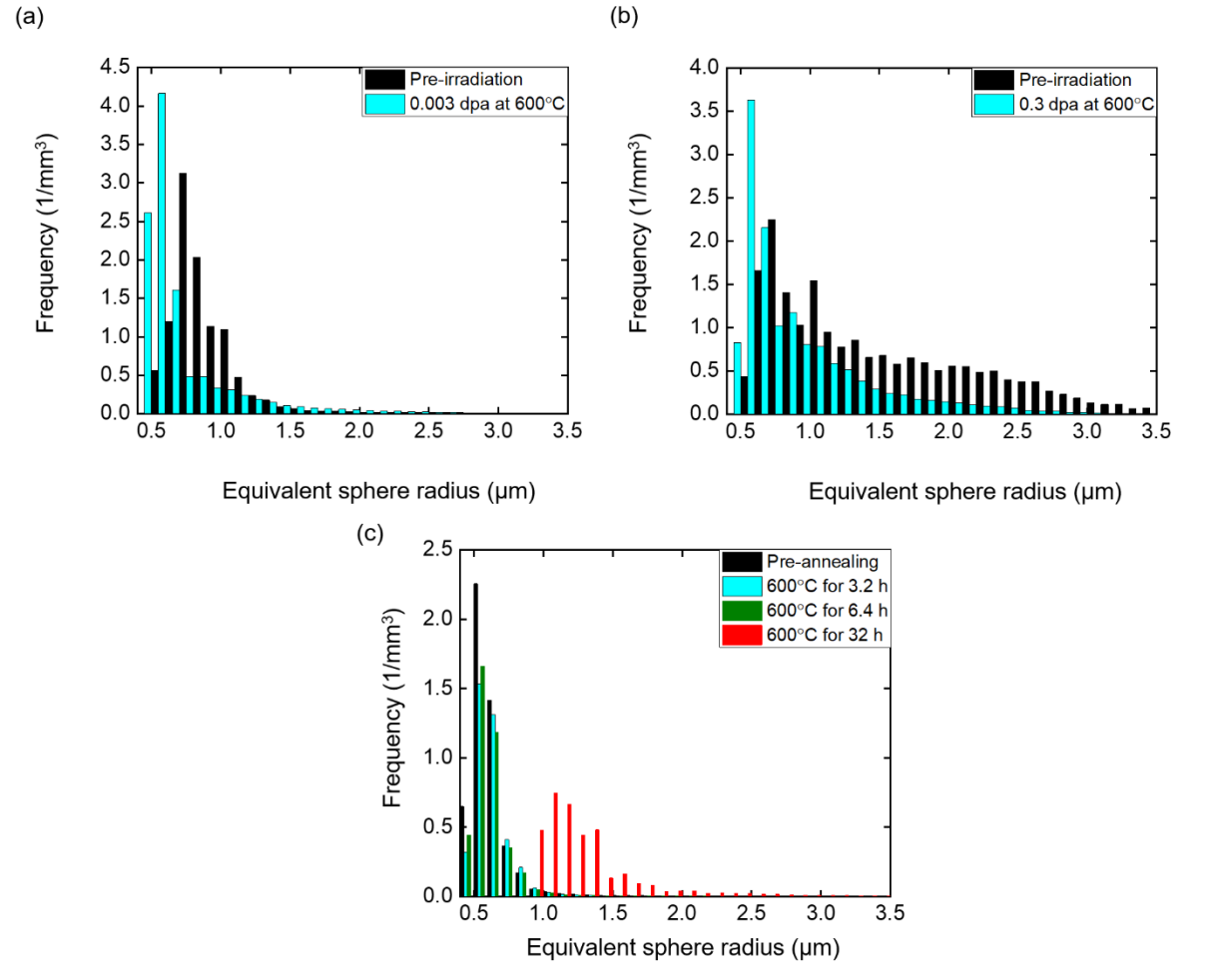

Figure 5. Frequency distributions of the equivalent sphere radii of precipitates in HT-UPS steel for (a) pre-irradiation and post-irradiation to 0.003 dpa at 600 °C and (b) pre-irradiation and post-irradiation to 0.3 dpa at 600°C. Frequency distributions of the equivalent sphere radii of the precipitates in the samples for (c) pre-annealing and post-annealing at 600 °C for 3.2 h, 6.4 h, and 32 h.

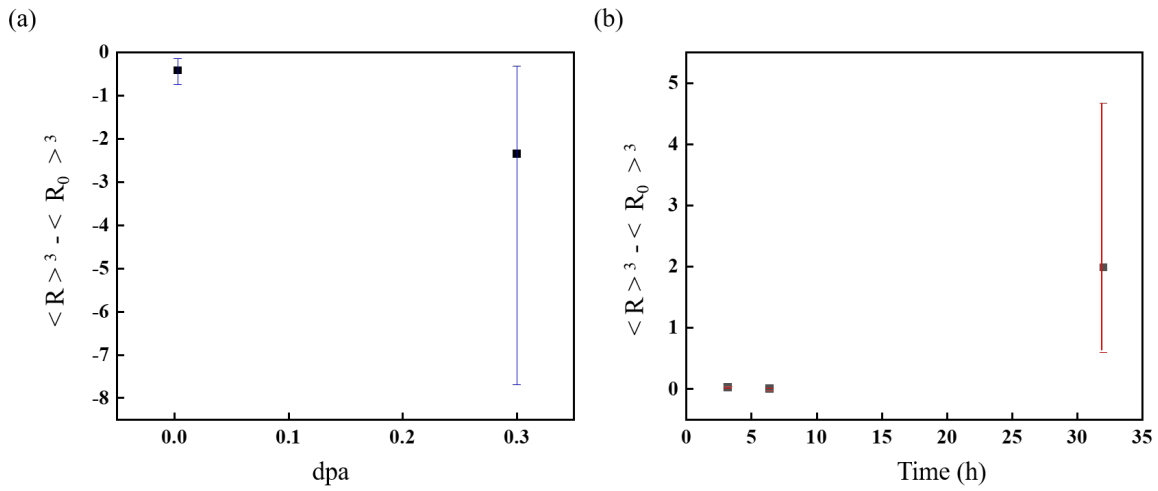

Figure 6. Evolution of the arithmetic mean precipitate radii for the HT-UPS steel specimens for (a) neutron irradiated to 0.003 dpa and 0.3 dpa at 600 °C and (b) annealed at 600 °C for 3.2 h, 6.4 h, and 32 h. The blue and red lines represent the upper and lower bounds of the standard deviations for (a) and (b), respectively.

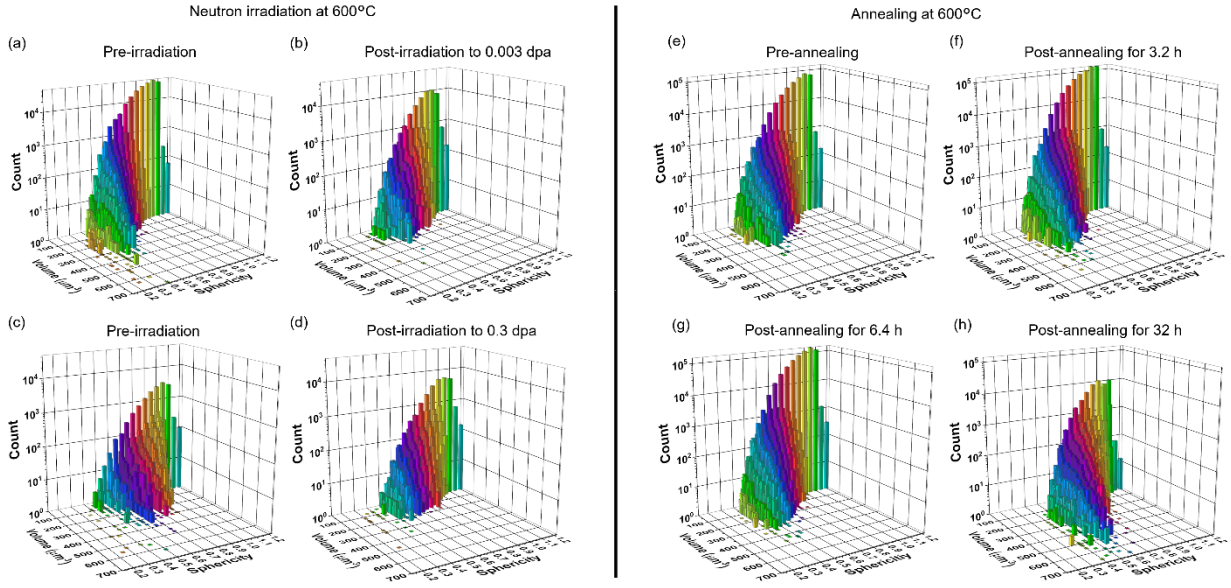

Figure 7. Bivariate distributions of precipitate volumes and sphericities in HT-UPS steel for (a) pre-irradiation and (b) post-irradiation to 0.003 dpa at 600°C, (c) pre-irradiation and (d) post-irradiation to 0.3 dpa at 600°C, and (e) pre-annealing and post-annealing at 600 °C for (f) 3.2 h, (g) 6.4 h, and (h) 32 h.

Table 1. Quantitative microstructural analysis of $Cr_{23}C_6$ precipitates in pre-irradiated and post-irradiated and pre-annealed and post-annealed HT-UPS steel. The first three columns refer to individual precipitate statistics while the last two comments refer to overall sample characteristics.

Specimen	Lognormal Mean Volume (μm^3) ± Standard Deviation	Average Volume (μm^3) ± Standard Deviation	Average Sphericity ± Standard Deviation	Volume Fraction (V_V)	Surface Area per Unit Volume (S_V) (mm^{-1})
Pre-irradiation	3.17±2.79	4.10±15.62	0.93±0.13	1.64%	45.90
0.003 dpa at 600°C	1.84±2.78	**3.01**±13.01	0.94±0.11	0.57%	15.22
Pre-irradiation	5.61±10.01	8.84±25.10	0.94±0.11	0.50%	9.20
0.3 dpa at 600°C	5.60±13.91	7.03±16.29	0.94±0.12	0.49%	10.83
Pre-annealing	1.19±0.96	1.69±6.81	0.95±0.11	1.02%	34.38
600 °C for 3.2hr	1.32±1.02	1.77±6.80	0.95±0.11	1.15%	40.20
600 °C for 6.4hr	1.21±0.91	1.59±5.96	0.95±0.11	1.23%	43.85
600 °C for 32hr	11.26±10.46	13.34±25.37	0.93±0.11	1.07%	19.73

Table 2. Chemical composition of HT-UPS steel.

Element	Fe	Ni	Cr	Mo	Mn	V	Ti	Nb	Si	C	P	N
Wt. %	65.25	16.00	13.91	2.59	2.00	0.53	0.28	0.11	0.11	0.06	0.04	0.02

Table 3. Synchrotron micro-computed tomography image acquisition parameters for in HT-UPS steel samples analyzed in this study, describing X-ray energy, quantity of views, pixel pitch, sample-to-detector distance, and the range of angles of rotation.

Specimen	Energy (keV)	Views	Pixel Pitch (μm)	Sample-to- detector distance (mm)	Rotation angular range
Pre-irradiation	64.0	601	0.746	70	0-360°
0.003 dpa at 600°C	71.7	1801	0.586	50	0-360°
Pre-irradiation	52.0	1801	0.746	70	0-360°
0.3 dpa at 600°C	71.7	1801	0.586	50	0-360°
Pre-annealing	71.7	1441	0.586	50	0-360°
600 °C for 3.2hr	71.7	1441	0.586	50	0-360°
600 °C for 6.4hr	71.7	1441	0.586	50	0-360°
600 °C for 32hr	71.7	3601	1.172	50	0-360°

Data Availability

The datasets generated during and/or analyzed during the current study are available from the corresponding author on reasonable request.

Declaration of competing interest statement

The authors declare that they have no known competing financial interests or personal relationships that could have appeared to influence the work reported in this paper.

Acknowledgments

This research was partially supported by Purdue University and the U.S Nuclear Regulatory Commission. This research used the resources of the Advanced Photon Source, a U.S. Department of Energy (DOE) Office of Science User Facility operated for the DOE Office of Science by Argonne National Laboratory under contract No. DE-AC02-06CH11357. This research was supported in part by the U.S. DOE Office of Nuclear Energy under DOE Idaho operations under Contract No. DE-AC07-051D14517.

References

[1] P. J. Maziasz, JOM 41, 14 (1989) https://doi.org/10.1007/BF03220265.

[2] P. J. Maziasz, JOM 70, 66 (2018) https://doi.org/10.1007/s11837-017-2642-x.

[3] P. J. Maziasz, D. N. Braski, A. F. Rowcliffe, (1989).

[4] P. J. Maziasz, R. L. Klueh, A. F. Rowcliffe, MRS Bull. 14, 36 (1989) https://doi.org/10.1557/S088376940006214X.

[5] Y. Yamamoto, M. P. Brady, Z. P. Lu, P. J. Maziasz, C. T. Liu, B. A. Pint, K. L. More, H. M. Meyer, E. A. Payzant, Science (80-.). 316, 433 (2007) https://doi.org/10.1126/science.1137711.

[6] M. C. Carroll, L. J. Carroll, Mater. Sci. Eng. A 556, 864 (2012) https://doi.org/10.1016/j.msea.2012.07.082.

[7] K. H. Lo, C. H. Shek, J. K. L. Lai, Mater. Sci. Eng. R Reports 65, 39 (2009) https://doi.org/10.1016/j.mser.2009.03.001.

[8] J. H. Shim, E. Kozeschnik, W. S. Jung, S. C. Lee, D. I. Kim, J. Y. Suh, Y. S. Lee, Y. W. Cho, Calphad Comput. Coupling Phase Diagrams Thermochem. 34, 105 (2010) https://doi.org/10.1016/j.calphad.2010.01.001.

[9] J. P. Shingledecker, P. J. Maziasz, N. D. Evans, M. J. Pollard, Int. J. Press. Vessel. Pip. 84, 21 (2007) https://doi.org/10.1016/j.ijpvp.2006.09.014.

[10] G. S. Was, Fundamentals of Radiation Materials Science: Metals and Alloys, Second Edition (2016) https://doi.org/10.1007/978-1-4939-3438-6.

[11] J. A. Todd, J.-C. Ren, Microstructural Studies of Advanced Austenitic Steels, ORNL/Sub/87-SA663C, 1989 (n.d.).

[12] W. Kesternich, J. Rothaut, J. Nucl. Mater. 104, 845 (1981) https://doi.org/10.1016/0022-3115(82)90705-X.

[13] S. J. Pawel, in *Fusion Sci. Technol.* (2012), pp. 369–374 https://doi.org/10.13182/FST12-A13447.

[14] C. Xu, W. Y. Chen, X. Zhang, Y. Wu, M. Li, Y. Yang, J. Nucl. Mater. 507, 188 (2018) https://doi.org/10.1016/j.jnucmat.2018.04.043.

[15] S. T. Nori, G. Park, W. Williams, Z. Lee, M. Warren, J. Terry, J.-S. Park, P. Kenesei, J. Almer, M. A. Okuniewski, J. Nucl. Mater. 554, 153056 (2021) https://doi.org/10.1016/j.jnucmat.2021.153056.

[16] X. Zhang, J. S. Park, J. Almer, M. Li, J. Nucl. Mater. 471, 280 (2016) https://doi.org/10.1016/j.jnucmat.2015.11.063.

[17] C. Xu, X. Zhang, Y. Chen, M. Li, J. S. Park, P. Kenesei, J. Almer, Y. Yang, Acta Mater. 156, 330 (2018) https://doi.org/10.1016/j.actamat.2018.07.008.

[18] J. Thomas, A. Figueroa Bengoa, S. T. Nori, R. Ren, P. Kenesei, J. Almer, J. Hunter, J. Harp, M. A. Okuniewski, J. Nucl. Mater. 537, 152161 (2020) https://doi.org/10.1016/j.jnucmat.2020.152161.

[19] S. Fidan, in *Micro-Computed Tomogr. Med. Eng.* (Springer International Publishing, 2020), pp. 267–276 https://doi.org/10.1007/978-3-030-16641-0_16.

[20] J. R. Parker, Algorithms for Image Processing and Computer Vision Second Edition (Wiley Publishing, Inc, 2011).

[21] T. F. Chan, L. A. Vese, IEEE Trans. IMAGE Process. 10, 266 (2001).

[22] D. Pedraza, P. Maziasz, in *Radiation-Induced Chang. Microstruct. 13th Int. Symp. (Part I)* (ASTM International, 2008), pp. 161-161–34 https://doi.org/10.1520/stp33816s.

[23] I. M. Lifshitz, V. V. Slyozov, J. Phys. Chem. Solids 19, 35 (1961) https://doi.org/10.1016/0022-3697(61)90054-3.

[24] C. Wagner, Zeitschrift für Elektrochemie, Berichte der Bunsengesellschaft für Phys. Chemie 65, 581 (1961) https://doi.org/10.1002/BBPC.19610650704.

[25] R. W. Balluffi, S. M. Allen, W. C. Carter, Kinetics of Materials: Balluffi/Kinetics (2005).

[26] S. J. Zinkle, P. J. Maziasz, R. E. Stoller, J. Nucl. Mater. 206, 266 (1993) https://doi.org/10.1016/0022-3115(93)90128-L.

[27] P. J. Maziasz, J. Nucl. Mater. 205, 118 (1993) https://doi.org/10.1016/0022-3115(93)90077-C.

[28] W. Kesternich, Philos. Mag. A Phys. Condens. Matter, Struct. Defects Mech. Prop. 77, 129 (1998) https://doi.org/10.1080/01418619808214234.

[29] T. M. Williams, J. M. Titchmarsh, D. R. Arkell, J. Nucl. Mater. 107, 222 (1982) https://doi.org/10.1016/0022-3115(82)90423-8.

[30] V. A. Pechenkin, G. A. Epov, Plasma Devices Oper. 3, 131 (1994) https://doi.org/10.1080/10519999408201809.

[31] V. A. Pechenkin, G. A. Epov, J. Nucl. Mater. 207(C), 303 (1993) https://doi.org/10.1016/0022-3115(93)90273-2.

[32] L. K. Mansur, M. R. Hayns, E. H. Lee, in *Met. Soc AIME.* (1981), pp. 359–382.

[33] S. T. Nori, A. Figueroa Bengoa, J. Thomas, H. Sharma, J. S. Park, R. Pokharel, J. Hunter, J. Almer, M. A. Okuniewski, Acta Mater. To be submitted (2021).

[34] W. Kesternich, R. V. Nandedkar, J. Nucl. Mater. 179–181, 1015 (1991) https://doi.org/10.1016/0022-3115(91)90263-7.

[35] S. Jin, L. Guo, F. Luo, Z. Yao, S. Ma, R. Tang, Scr. Mater. 68, 138 (2013) https://doi.org/10.1016/j.scriptamat.2012.10.002.

[36] H. Wollenberger, J. Nucl. Mater. 216, 63 (1994) https://doi.org/10.1016/0022-3115(94)90007-8.

[37] J. A. Todd, J. C. Ren, Mater. Sci. Eng. A (1989) https://doi.org/10.1016/0921-5093(89)90106-8.

[38] T. Sourmail, Mater. Sci. Technol. 17, 1 (2001) https://doi.org/10.1179/026708301101508972.

[39] H. Sahlaoui, K. Makhlouf, H. Sidhom, J. Philibert, Mater. Sci. Eng. A 372, 98 (2004) https://doi.org/10.1016/j.msea.2003.12.017.

[40] A. Gharehbaghi, M. Selleby, Precipitation Study in a High Temperature Austenitic Stainless Steel Using Low Voltage Energy Dispersive X-Ray Spectroscopy (2012).

[41] N. Terao, B. Sasmal, Metallography 13, 117 (1980) https://doi.org/10.1016/0026-0800(80)90010-5.

[42] H. U. Hong, B. S. Rho, S. W. Nam, Mater. Sci. Eng. A 318, 285 (2001) https://doi.org/10.1016/S0921-5093(01)01254-0.

[43] Q. Xiong, J. D. Robson, L. Chang, J. W. Fellowes, M. C. Smith, J. Nucl. Mater. 508, 299 (2018) https://doi.org/10.1016/j.jnucmat.2018.05.074.

[44] C. Xu, W. Y. Chen, Y. Chen, Y. Yang, J. Nucl. Mater. 509, 644 (2018) https://doi.org/10.1016/j.jnucmat.2018.07.044.

[45] D. R. Harries, A. C. Roberts, in *Eff. Radiat. Struct. Met.* (1967), pp. 21–47 https://doi.org/10.1520/stp41316s.

[46] J. L. McDuffee, G. L. Bell, R. J. Ellis, R. W. Hobbs, L. L. Snead, M. Okuniewski, in *Proc. 2014 Water React. Fuel Perform. Meet. Top Fuel / LWR Fuel Perform. Meet. (WRFPM 2014)* (Sendai, Japan, 2014), paper 100084.

[47] J. Hunter, D. W. Brown, M. Okuniewski, Can. Inst. Non-Destructive Evol. J. 36, 12 (2015).

[48] J. H. Hubbell, S. M. Seltzer, *NIST* (2004) https://doi.org/http://physics.nist.gov/xaamdi.

[49] J. Hunter, T. Ickes, B. Lattimore, Title : Overview of Tomography Developments at LANL (n.d.).

[50] T. M. Buzug, Computed Tomography: From Photon Statistics to Modern Cone-Beam CT (2010) https://doi.org/10.1007/978-3-540-39408-2.

[51] G. V S Raj Kumar, V. R. Kumar Reddy, M. Jogendra Kumar, G. Raj Kumar, R. Vijay Kumar Reddy, Int. J. Sci. Res. Eng. Technol. 3, 992 (2014).

[52] W. Khan, Int. J. Futur. Comput. Commun. 3, 89 (2014) https://doi.org/10.7763/IJFCC.2014.V3.274.

[53] P. J. Withers, C. Bouman, S. Carmignato, V. Cnudde, D. Grimaldi, C. K. Hagen, E. Maire, M. Manley, A. Du Plessis, S. R. Stock, Nat. Rev. Methods Prim. 1, 18 (2021) https://doi.org/10.1038/s43586-021-00015-4.

[54] A. Snigirev, I. Snigireva, V. Kohn, S. Kuznetsov, I. Schelokov, Rev. Sci. Instrum. 66, 5486 (1995) https://doi.org/10.1063/1.1146073.

[55] G. Lehmann, D. Legland, G. Lehmann, Efficient N-Dimensional Surface Estimation Using Crofton Formula and Run-Length Encoding (2012).

[56] W. E. Lorensen, H. E. Cline, in *Proc. 14th Annu. Conf. Comput. Graph. Interact. Tech. SIGGRAPH 1987* (Association for Computing Machinery, Inc, 1987), pp. 163–169 https://doi.org/10.1145/37401.37422.

[57] J. Thomas, S. T. Nori, A. Figueroa, R. Ren, M. A. Okuniewski, P. Kenesei, J. Sang-Park, J. Almer, J. Harp, in *Trans. Am. Nucl. Soc.* (American Nuclear Society, 2018), pp. 1406–1407.

[58] C. Chuang, D. Singh, P. Kenesei, J. Almer, J. Hryn, R. Huff, Scr. Mater. 106, 5 (2015) https://doi.org/10.1016/j.scriptamat.2015.03.017.